EXPERIENCES ON ACTUATOR FAULT DETECTION, DIAGNOSIS AND ACCOMMODATION FOR ROVS

M. Caccia, R. Bono, Ga. Bruzzone, Gi. Bruzzone, E. Spirandelli, G. Veruggio

Consiglio Nazionale delle Ricerche - Istituto Automazione Navale

Via De Marini, 6
16149 Genova, Italy
E-mail: { max, ric, gabry, gio, edo, veruggio } @ ian.ge.cnr.it

Abstract

This paper addresses the problem of low cost actuator fault detection, diagnosis and accommodation for Remotely Operated Vehicles. The research is based on the analysis of the telemetry of Romeo, the over-actuated ROV developed by C.N.R.-I.A.N., operating both in nominal and different failure conditions. Results demonstrate how the monitoring of the servo-amplifiers' I/O variables enables the detection and diagnosis of actuator faults for operating ROVs, supporting the pilot in making decisions on the real-time reconfiguration of the propulsion system. The integration of the servo-level FDDA module with a conventional navigation, guidance and control system is discussed. On the basis of experienced time-varying effects of operating failures, suitable models of the damaged actuators and algorithms for the generation of fault symptoms and alarms have been designed, implemented and satisfactorily tested on a large amount of recorded ROV data. The conventional fault accommodation procedure based on the reconfiguration of the vehicle's thrust control matrix has been applied. The capability of Romeo of working in a reduced actuation configuration has been operationally demonstrated executing shallow water benthic missions for scientific users.

Introduction

Currently, unmanned underwater vehicles (UUVs) can satisfactorily perform a large amount of scientific missions for oceanographic surveys, exploration of unknown areas and operations in the proximity of the seabed or man-made underwater structures. As discussed in [1], at this stage the main technical issue is to improve the system reliability in order to guarantee the mission is accomplished even in the presence of some variations from the nominal conditions, i.e. faults. In this sense, fault management systems for UUVs able to detect, isolate and accommodate faults, have been investigated and designed in order to improve the vehicle degree of autonomy, reliability and capability of performing missions in harsh environments.

UUVs' operations can be affected by two kinds of faults: failures in the hardware and software subsystems of the vehicle, such as thruster seizing or sensor breaking, and unforeseen environmental conditions, which could jeopardize the working mode of the sensors measuring the vehicle-environment interactions, such as multi-path phenomena affecting echo-sounders' performances. In the past, attention focused on the vehicle faults, distinguishing between actuator and sensor faults, and trying to classify the expected system failures on the basis of their probable response as reported in [2], where zero-response breaking, permanent offset jamming, intermittent slipping, decreasing response creeping failure and random control failure damages have been listed.

In the nineties, theoretical advancements in fault diagnostics obtained in various fields of applications, from aeronautical and aerospace systems to nuclear and chemical plants, have been transferred to underwater robotics. Since unmanned underwater vehicles can be modeled by a small number of state variables, model-based techniques for fault detection have been preferred to model-free ones. In particular, fault detection techniques based on parameter estimation and analytical redundancy, i.e. the same quantity is calculated by combining data from different sensors or model-based predictors, have been developed. An example of black-box identification combined with gradient filtering to generate failure events is given in [2], while a technique to manage analytical redundancy through expert systems' rules is presented in [3]. In [1] and [4], a model-based observer is used to generate a residual between the sensor measured values and that predicted from the model in order to detect dynamic faults. A fault is detected when the residual magnitude is higher than a suitable threshold for more than a fixed length of time. The same method to avoid false alarms, after processing residuals generated through analytical redundancy, is used in [5], where an accommodation technique for thruster failures is also presented in the case of an over-actuated vehicle. Modeled actuator faults can be detected and isolated through a bank of extended Kalman filters or sliding-mode observers as discussed in [6] and [7]. Due to the difficulties of having available recorded telemetry data of UUV actual faults, the above mentioned investigations are based on simulations of plant damages of the types classified in [2]. In particular, in [3] failure detection is performed on the heading and depth control surfaces and sensors of a simulated torpedo-like AUV. The Rae and Dunn's failure detection system has been tested and evaluated on the simulator of the Ocean Voyager AUV in the case of speed sensor slipping and jamming, depth-meter breaking and compass jamming [2]. In the same way, the model-based observer approach presented in [1] has been tested by simulating a stern plane fault in the presence of wave disturbances using a model of the US Navy DSRV vehicle. On the other hand, Yang et al. and Alessandri et al. simulated thruster and sensor failures suitably programming the actuation and acquisition system of actual vehicles, Odin [5], Roby2 [6] and Romeo [7] respectively, operating in water. A full-stroke fin fault has been simulated on the 21UUV vehicle during steering maneuvers in [4]. High accuracy navigational instruments, which afforded full state feedback observers, made possible the evaluation of model-based residuals after nonlinear optimization of the model and Kalman filter parameters. Anyway, only time-invariant actuator faults have been considered.

In the following, research focusing on the design of fault detection, diagnosis and accommodation (FDDA) systems based on operationally experienced faults in ROV actuators is presented. The main goal is to design a fault management system for unmanned underwater vehicles, able to satisfy the basic requirement of "detecting and diagnosing experienced failures", supporting the supervision module, i.e. the ROV human operator during tele-operation, in reconfiguring the system if required. In addition, the fault management system has to be easily integrated in the hierarchical control architectures, which characterize a large number of advanced UUVs [8]. This requirement involves the development of fault detection and isolation modules at the various levels of the control architecture, such as servo-amplifiers, model-based dynamics and steady-state monitoring, resulting in a reliable diagnostics system based on information redundancy. Operational experience, ripened during the under-ice missions of the Romeo ROV in the XIII Italian expedition to Antarctica in 1997-98 [9] and the ARAMIS project's trials in the thermal vent areas near the island of Milos in the Aegean Sea [10], revealed the permanent time-varying multiplicative effects of flooded thruster failures and the stationary zero-output effects of rotor failures. The time-varying multiplicative nature of many experienced thruster faults, combined with the vehicle model uncertainty and the unavailability of linear velocity and acceleration measurements, e.g. in the case of the ROV heave motion only noisy depth measurements were available, has made it difficult to generate robust observer-based residual during closed-loop operations and suggested the execution of pre-defined steady-state maneuvers specifically designed to solve ambiguities in the presence of position measurements only [11].

The research presented in the following demonstrates how low cost servo-amplifiers' monitoring enables the detection and diagnosis of actuator faults for operating ROVs, supporting the pilot in making decisions on the real-time reconfiguration of the propulsion system. Thruster fault accommodation can be easily performed by reconfiguring the Thrust Control Matrix in the case of overactuated UUVs [5] [12]. All the work has been supported by the ROV telemetry data collected during Romeo's at sea operations in Antarctica and in the Aegean Sea.

System architecture

In conventional advanced UUV control architectures, a NGC loop computes the force and torque ϕ^* that the actuation system has to apply to the vehicle on the basis of the errors between the desired and estimated operational variables χ, e.g. absolute or environment-related positions, and/or speeds ξ. The desired control action ϕ^* is mapped onto the actuator thrusts τ^* by the Thrust Control Matrix, which, in the case of over-actuated vehicles, allows the selection of a suitable mapping mode μ^*. The computation of the reference thruster revolution rates n* is immediate by inverting the actuator I/O relationships taking into account the propeller-hull interactions. See [12] for a detailed discussion of the Romeo's hierarchical guidance and control architecture. Thruster speeds, as well as exerted thrusts, are controlled by servo-amplifiers, closing servo-velocity loops with time constants generally negligible with respect to the overall system. Thus, each actuator can be represented as a sub-system, constituted by the servo-amplifier, electrical motor and propeller, and the actuator's behavior can be monitored by observing the servo-amplifier's I/O variables, i.e. the desired propeller revolution rate and any variable related to the motor speed (e.g., the current i_{mot} which actually circulates in the motor in the case of Romeo). On the basis of the monitoring of the servo-amplifiers I/O variables, the Fault Detection and Diagnosis module can isolate actuator failures and signal them to the Fault Accommodation module, e.g. the ROV human pilot, that can select a suitable mapping of the control action onto the actuator thrusts. The resulting NGC and servo-level FDDA system architecture is shown in Figure 1.

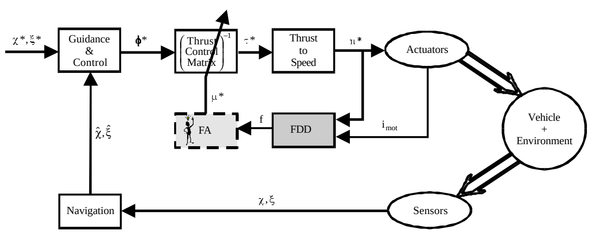

Figure 1. NGC and servo-level FDDA system architecture.

Romeo: mechanical design and actuation system

The Romeo ROV has been designed and developed by the Robotics Dept. of the Institute for Ship Automation of the Italian National Research Council for scientific applications and research in the field of intelligent vehicles. Its mechanical design follows the structure of the last generation scientific ROVs, such as Victor 6000 [13] and Tiburon [14]. The vehicle is constituted by three sections: on the bottom an interchangeable toolsled for scientific devices is connected to the basic frame, the foam for buoyancy is positioned on the top, while in the middle section, the basic frame carries on a number of titanium canisters for control and communication electronics, power supply system, sensors and actuators as shown in Figure 2. The resulting ROV is about 1 m in height, 0.9 m in width and 1.3 m in length, weighs about 450 kg in air and is intrinsically stable in pitch and roll. More detailed information about Romeo computer and software design, and exploitation can be found in [15].

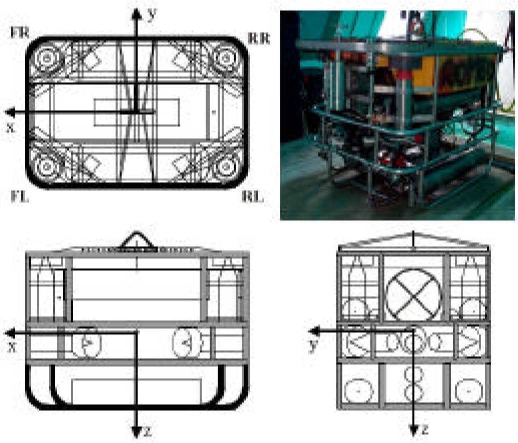

Figure 2. Romeo mechanical design

The Romeo's actuation system consists of eight thrusters arranged two by two in the corners, with the horizontal ones parallel to the diagonals of the *xy* section. This fault-tolerant thruster configuration uncouples the horizontal control of surge, sway and yaw, from the vertical control of roll, pitch and heave.
Each Romeo's thruster consists of a titanium cylindrical pressure vessel containing a MAE M644-2530 DC motor (60 V @ 300 W) with the corresponding tachometer and rotary joint (see Figure 3).

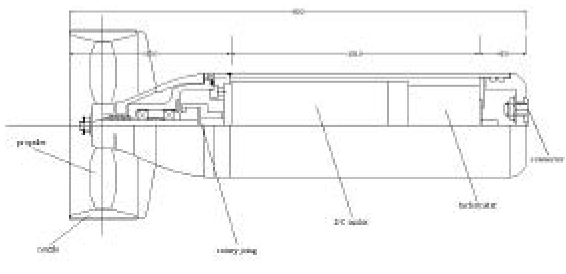

Figure 3. Romeo actuator mechanical design

The propeller, positioned inside its nozzle, has three blades with asymmetric camber in order to minimize the reduction in efficiency due to interactions with the thruster canister. A rotary graphite-ceramic seal makes the thruster watertight. Each DC motor is controlled by a Mini Maestro DCD60V servo-amplifier, located in the main ROV canister, which performs a PID control of the thruster velocity on the basis of the error between the signal of the motor tachometer and the reference speed. The servo-amplifier provides a digital output signaling the activation of any protection or current limitation, and an analog output signal proportional to the current i_{mot} which actually circulates in the motor.

Actuator model

Nominal model

As discussed in [16], in the case of low speed ROVs in many standard operational conditions the dependence of the propeller thrust on the advance speed as well as the time constant of the servo velocity loop of the controlled thruster system can be neglected, as widely accepted in the literature, and the propeller thrust may be modelled as $\tau(n) \cong c_\tau n|n|$, where c_τ is a positive constant and n is the propeller revolution rate.
The torque exerted by a rotating propeller at bollard conditions is

$$Q(n) \cong Q_{|n|n} |n| n \qquad (1),$$

while the DC motor dynamics is described by equations:

$$\begin{aligned} L_a \frac{di_a}{dt} &= -R_a i_a - 2\pi K_M n + u_a \\ 2\pi J_m \frac{dn}{dt} &= K_M i_a - Q(n) \end{aligned} \qquad (2),$$

where i_a, L_a, R_a and u_a are the armature current, inductance, resistance and voltage, K_M is the motor torque constant, J_m is the moment of inertia of motor and thruster, and Q(n) is the load from the propeller. In steady-state conditions $K_M i_a = Q(n)$, and substituting in eqn. (1), $i_a \propto |n| n$, $\frac{i_a}{|n| n} \cong \text{const}$, i.e. the armature current is proportional to the signed square of the propeller revolution rate, that is to the propeller thrust.
The signal i_a is almost equal to i_{mot} , i.e. the current circulating in the motor, which, in steady-state conditions, can be linked to the generic j-th motor revolution rate as it follows:

$${}_j i_{mot} \cong {}_j k_{n|n|} \; {}_j n |{}_j n| + {}_j k_0 \qquad (3)$$

where ${}_j k_0$ is the current absorbed by the thruster at rest. The subscript j indicating the actuator index will be omitted in the following when a generic actuator will be dealt with. It is worth noting that in nominal conditions the propeller revolution rate n coincides with the desired one n* but for a negligible time constant.

Thruster I/O relationship identification

Experiments have been carried out to identify the current-speed coefficients $[k_{n|n|} \quad k_0]$. The vehicle's vertical thrusters have been excited with a square wave signal of the reference propeller revolution rate and the corresponding motor currents i_{mot} of the four vertical thrusters have been measured with a 10 Hz sampling rate as shown in Figure 4a where results from the Antarctic mission are reported. In order to handle the high noise in the acquired current signals and the fact that eqn.(3) decreases its validity with the increase of the variations in the reference motor velocity, a band-shaped relationship between the propeller's reference revolution rate and the measured motor current has been identified, i.e. $i_{mot}^{min}\left(\underline{k}_{mot}^{min}, n^*\right) \le i_{mot}(n^*) \le i_{mot}^{max}\left(\underline{k}_{mot}^{max}, n^*\right)$.

First the mean and standard deviation of the measured motor currents have been computed for a set of 10 seconds data sequences, i.e. 100 samples, corresponding to the steady-state reference propeller revolution rates.

Figure 4. Thruster identification experiment for Romeo's Antarctic mission (vertical front left thruster)

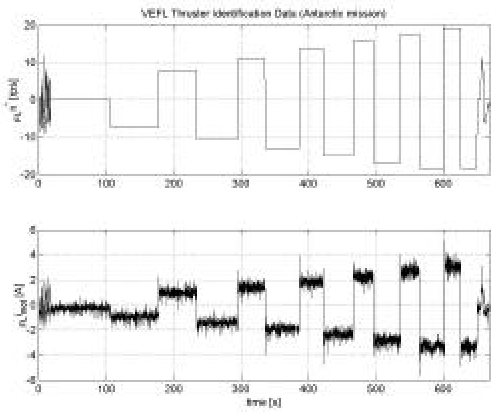

Figure 4a. Top: propeller's reference revolution rate; bottom: measured motor current.

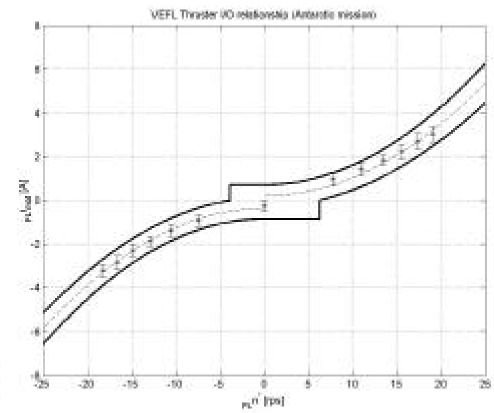

Figure 4b. Estimated I/O relationship: motor current vs. propeller's reference revolution rate

Examples of the results are plotted in Figure 4, where the asterisks indicates the estimated working points $\left(n^*, \bar{i}_{mot}\right)$ and the error bar ranges are equal to the signal standard deviations $\sigma_{i_{mot}}$. Secondly the upper and lower bounds, $i_{mot}^{max}(n^*)$ and $i_{mot}^{min}(n^*)$, of the I/O relationships have been determined by a Least Square identification of the model given by eqn.(3) with the observation points $\left\{n^*, \bar{i}_{mot} + 2\sigma_{i_{mot}}\right\}$ and $\left\{n^*, \bar{i}_{mot} - 2\sigma_{i_{mot}}\right\}$ respectively. The procedure has been applied separately for the positive and negative revolution rates of each thruster.

Results are reported in Figure 4b, where the bound functions are plotted in bold-face. It is worth noting that, in order to face the high uncertainty in the motor current measurements, $i_{mot}^{min}(n^*)$ and $i_{mot}^{max}(n^*)$ assume constant values for low reference revolution rates as it follows:

$$i_{mot}^{max}(n^*) = \begin{cases} {}^{-}k_{n|n|}^{max}\, n^*|n^*| + {}^{-}k_0^{max}, & n^* < {}^{-}\tilde{n} \\ {}^{+}k_0^{max}, & {}^{-}\tilde{n} \le n^* \le 0 \\ {}^{+}k_{n|n|}^{max}\, n^*|n^*| + {}^{+}k_0^{max}, & n^* > 0 \end{cases}$$

$${}^{-}\tilde{n} = \min\left\{{}^{-}\bar{n}, {}^{-}n_0\right\}, \; {}^{-}n_0 : {}^{-}k_{n|n|}^{max}\; {}^{-}n_0 \left|{}^{-}n_0\right| + {}^{-}k_0^{max} = 0$$

$$i_{mot}^{min}(n^*) = \begin{cases} {}^{-}k_{n|n|}^{min}\, n^*|n^*| + {}^{-}k_0^{min}, & n^* < 0 \\ {}^{-}k_0^{min}, & 0 \le n^* \le {}^{+}\tilde{n} \\ {}^{+}k_{n|n|}^{min}\, n^*|n^*| + {}^{+}k_0^{min}, & n^* > {}^{+}\tilde{n} \end{cases}$$

$${}^{+}\tilde{n} = \max\left\{{}^{+}\bar{n}, {}^{+}n_0\right\}, \; {}^{+}n_0 : {}^{+}k_{n|n|}^{min}\; {}^{+}n_0 \left|{}^{+}n_0\right| + {}^{+}k_0^{min} = 0$$

(4)

where ${}^{+}\bar{n}$ and ${}^{-}\bar{n}$ have been heuristically assumed equal to 3.5 rps and –3.5 rps respectively.

Experienced actuator fault models

<u>Thruster blocking</u>

When the thruster is blocked by an external action, e.g. a solid body between the blades of the propeller, the motor tries to increase the exerted torque in order to counteract the disturbance, i.e. a current higher than a maximum threshold could be requested by the PID control of the motor speed. In this case, the Mini Maestro DCD60V servo-amplifier delivers the maximum current for about two seconds, then a current limitation to the nominal value is forced and this event is signaled by the activation of the protection digital output. Thus, the servo-amplifier detects and signals thruster failures characterized by $|n| \cong 0$ and $|i_{mot}| >> \left|k_{n|n|} n^* |n^*| + k_0\right|$.

Such a behavior has been noticed during the 1997-'98 Antarctic mission when a block of ice blocked the blades of a Romeo's vertical thruster during surface docking operations. The servo-amplifier reached the current limitation working mode, which was signaled to the ROV pilot, who could disable the thruster and enable it again when the ice block melted.

Flooded thruster

Actuator I/O behavior in the case of Romeo's vertical front left thruster flooding during the 1997-'98 Antarctic campaign is shown in Figures 5a and 5b.

Figure 5. Vertical front left thruster flooding during Antarctic mission.

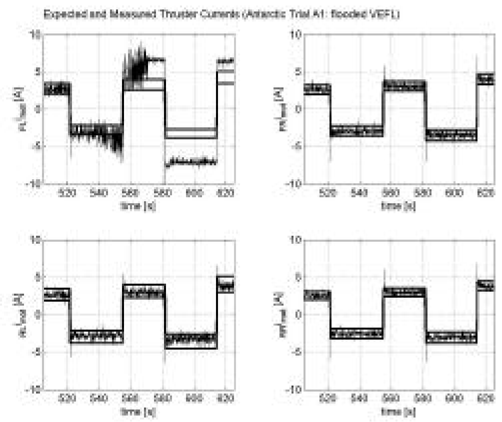

Figure 5a. From top-left clockwise: expected and measured vertical front-left, front-right, rear-right and rear-left motor current.

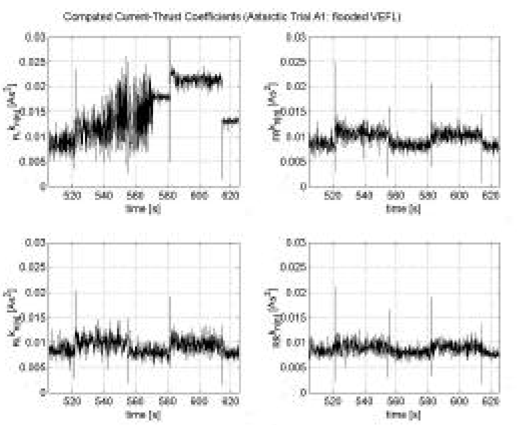

Figure 5b. From top-left clockwise: computed vertical front-left, front-right, rear-right and rear-left current-speed coefficient.

Figure 5a shows the measured and expected Romeo's vertical motor currents when flooding occurred. Flooding effects started to show after about 540 s and clearly stabilized at time of about 570 s. It is clearly visible the higher current with respect to the nominal value absorbed by the flooded thruster, as well as the current spikes required to track step variations in the reference thruster velocities. The rough estimates of the current-thrust coefficients $k_{n|n|}$, computed as $k_{n|n|} \cong \frac{i_{mot}}{n^*|n^*|}$, are plotted in Figure 5b. As shown by the vertical front-left computed coefficient in the top-left plot, in particular in the time intervals from 570 s to 580 s and from 618 s, the effects of the flooding are time-varying.

The presence of water inside the thruster modifies the internal electrical connections. In particular, the salt water caused an electrical dispersion, which reduced the feed-back signal n_m of the motor revolution rate n from the tachometer to the servo-amplifier, i.e. $n_m = \lambda n, 0 \le \lambda < 1$. In these conditions, when the servo-amplifier forced the feed-back signal n_m to track the desired speed n^*, the actual speed n was higher than the desired one, i.e. $n \to \frac{1}{\lambda} n^*$. Since at bollard conditions, the thrust τ delivered by a propeller is $\tau(n) \cong c_\tau n|n|$, the magnitude of the actual force of the flooded thruster $\tau \cong \frac{1}{\lambda^2} c_\tau n^*|n^*| = \frac{1}{\lambda^2}\tau^*$ was higher than the desired one. In the same way, the armature current i_a as well as the motor current i_{mot} increased proportionally to the square of the propeller revolution rate, i.e. $i_a \cong \frac{1}{\lambda^2} k|n^*|n^*$ and $i_{mot}(n^*) \cong \frac{1}{\lambda^2} k_{n|n|} n^*|n^*| + k_0$.

Rotor failure

Thruster I/O behavior in the case of Romeo's vertical rear right rotor failure during the 2000 ARAMIS campaign in the Aegean Sea is shown in Figures 6a and 6b. As clearly shown in the top picture of Figure 6a and in Figure 6b, the fault, occurred after about 3524 s, determined the zeroing of the motor current, i.e. a dramatic reduction of the current-thrust coefficient $k_{n|n|}$. The bottom picture of Figure 6a shows the thruster behavior in nominal conditions, pointing out the presence of current spikes corresponding to the PID control action required to track fast variations in the reference thruster velocity.

As revealed by the inspection of the thruster after the mission, a metal fragment broke off the stator magnet, probably as a consequence of a previous mechanical trauma, and cut about the 40% of the wires of the rotor coil winding. As a consequence the motor could stop, and in that case, it could start again if an external action allowed it to exceed the dead center corresponding to the cut coils.

The effects of the rotor failure are the zeroing of the actual speed n, the thruster thrust τ and the motor current i_{mot}, i.e. $i_{mot}(n^*) \cong 0$.

Figure 6. Vertical rear right rotor failure during ARAMIS Aegean Sea mission.

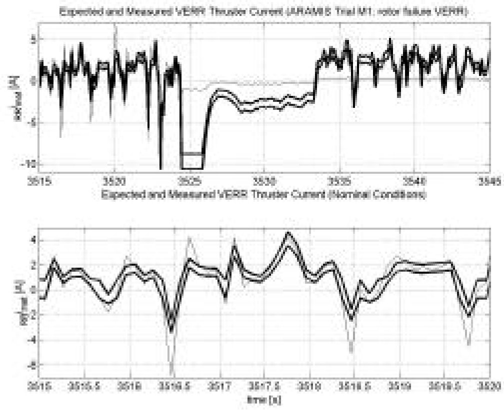

Figure 6a. Expected and measured vertical rear right motor current. Top: before and after the rotor failure; bottom: particular of the nominal behavior.

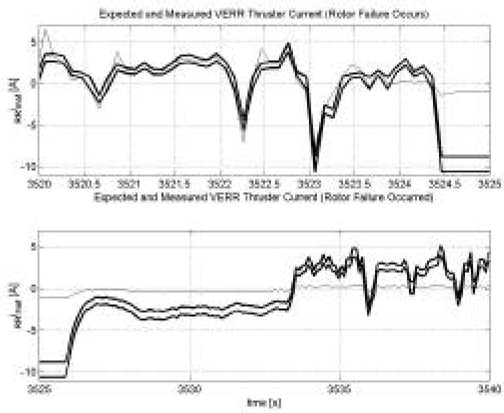

Figure 6b. Expected and measured vertical rear right motor current. Top: particular on the failure occurrence; bottom: particular of the rotor failure behavior.

Fault detection and diagnosis

Fault symptoms and alarms generation

On the basis of the experienced actuator failures during Romeo's operations, the behavior of the motor current with respect to the required propeller revolution rate can be classified as shown in Figure 7.

The $\langle n^*, i_{mot} \rangle$ plane can be divided in a region of *nominal behavior*, i.e. $N = \{(n^*, i_{mot}) : i_{mot}^{min}(n^*) \le i_{mot} \le i_{mot}^{max}(n^*)\}$, two regions indicating a *high gain fault* where the motor current is higher in module and of the same sign of the expected one, as in the case of thruster flooding, and two regions of *small gain fault* where the motor current module is lower than the expected one, as in the case of rotor failure. For the sake of completeness a couple of regions of *negative gain fault* have been introduced, where the motor current sign is the opposite of the expected one. This operating condition has not been experienced with Romeo and could indicate an inversion in the connections of the wires of the reference signal or of the tachometer. It is worth noting that *small gain faults* are not observable for low reference motor velocities.

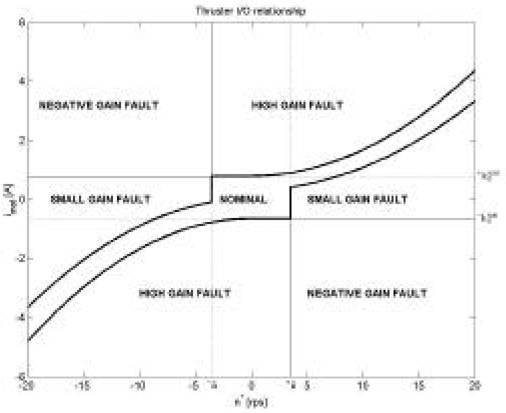

Figure 7. Nominal behavior and fault regions in the reference motor velocity - motor current plane.

Thus the fault symptoms at time t can be computed as it follows:

$$S_{HGF}(t) = \left[\left(i_{mot}(t) > i_{mot}^{max}(t)\right) \wedge \left(n^*(t) \ge {}^{-}\tilde{n}\right)\right] \vee \left[\left(i_{mot}(t) < i_{mot}^{max}(t)\right) \wedge \left(n^*(t) \le {}^{+}\tilde{n}\right)\right] \quad (5),$$

$$S_{SGF}(t) = \left[\left(i_{mot}^{max}(t) < i_{mot}(t) \le {}^{+}k_0^{max}\right) \wedge \left(n^*(t) < {}^{-}\tilde{n}\right)\right] \vee \left[\left({}^{-}k_0^{min} \le i_{mot}(t) < i_{mot}^{min}(t)\right) \wedge \left(n^*(t) > {}^{+}\tilde{n}\right)\right]$$

(6),

and

$$S_{NGF}(t) = \left[\left(i_{mot}(t) > {}^{+}k_0^{max}\right) \wedge \left(n^*(t) < {}^{-}\tilde{n}\right)\right] \vee \left[\left(i_{mot}(t) < {}^{-}k_0^{min}\right) \wedge \left(n^*(t) > {}^{+}\tilde{n}\right)\right] \quad (7).$$

Since the measurements $i_{mot}(t)$ are quite noisy, fault alarms are generated by thresholding the persistence degrees of the symptoms in a *fault-observation* sliding window of width N Δt [17]. Persistence degrees of the symptoms are computed as:

$$p_{HGF}(t) = \frac{\sum_{i=0}^{N-1} S_{HGF}(t - i\Delta t)}{N},$$

$$p_{SGF}(t) = \frac{\sum_{i=0}^{N-1} S_{SGF}(t - i\Delta t)}{N} \quad \text{and}$$

$$p_{NGF}(t) = \frac{\sum_{i=0}^{N-1} S_{NGF}(t - i\Delta t)}{N} \quad (8).$$

To reduce the effects of the measurement noise, a differential persistence degree of the *high* and *small gain* symptoms has been defined as it follows:

$$p_{HSGF}(t) = p_{HGF}(t) - p_{SGF}(t) = \\ = \frac{\sum_{i=0}^{N-1} S_{HGF}(t - i\,\Delta t) - \sum_{i=0}^{N-1} S_{SGF}(t - i\,\Delta t)}{N} \qquad (9).$$

Fault alarms $f_{HGF}(t)$ and $f_{SGF}(t)$ at time t can be generated if $p_{HSGF}(t) > p_{HSGF}^{thr}$ and $p_{HSGF}(t) < -p_{HSGF}^{thr}$ respectively.

The persistence degrees of the *high* and *small gain* symptoms in the cases of flooded thruster and rotor failure seen in section 4.2 are plotted in Figures 8 and 9 respectively.

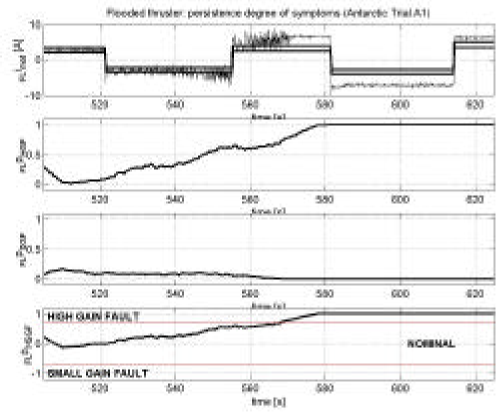

Figure 8. Vertical front left thruster flooding during Antarctic mission. From top to bottom: measured and expected motor current, and persistence degree of the high, small and high-small gain symptoms.

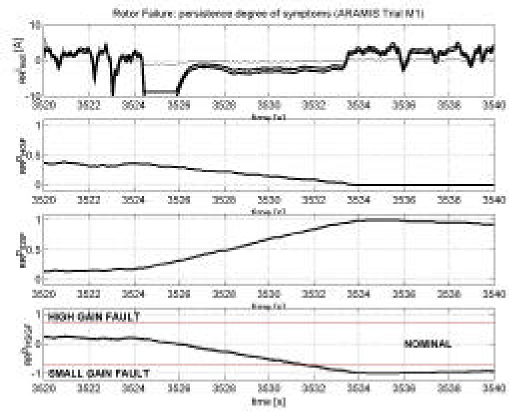

Figure 9. Vertical rear right rotor failure during ARAMIS Aegean Sea mission. From top to bottom: measured and expected motor current, and persistence degree of the high, small and high-small gain symptoms.

No *negative gain fault* symptoms have been revealed. As shown in the figures, the faults have been properly detected adopting a sliding window of width 10 s, i.e. 100 samples at 10 Hz, and an alarm threshold p_{HSGF}^{thr} equal to 0.7. The alarm threshold is rather high to reduce the number of false alarms originated by the measurement noise and the rough approximation of the model given by eqn. (3) during transients. This aspect is quite important because, when a failure is detected, the damaged actuator is usually switched off and no more activated during the mission.

Observability of the faults

As discussed before, see Figure 7, small gain faults are not observable for low reference motor velocities. As a consequence of this fact, no fault alarms are generated by monitoring a failed-rotor actuator if the desired propeller revolution rate is about zero in a large number of instants in the *fault-observation* sliding window of width N Δt. An example is given in Figure 10, where in the time interval between 6965 s and 6990 s zero speed has been required to the Romeo's vertical rear right actuator, whose rotor was damaged.

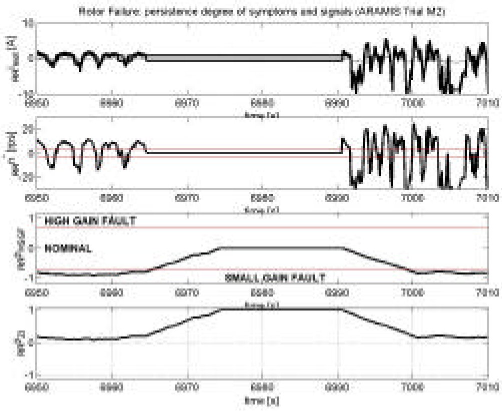

Figure 10. Vertical rear right rotor failure during ARAMIS Aegean Sea mission. From top to bottom: measured and expected motor current, reference propeller revolution rate, persistence degree of the *high-small gain* symptom and *zero input* signal.

As shown in the third picture from the top, the persistence degree of the failure symptom gets zero when the system is not excited. Anyway, information about the observability of *small gain faults* can be easily collected defining a *signal of zero input* s_{ZI} and its persistence degree p_{ZI} as it follows:

$$s_{ZI}(t) = \left({}^{-}\tilde{n} \le n*(t)\right) \wedge \left(n*(t) \le {}^{+}\tilde{n}\right) \quad \text{and}$$

$$p_{ZI}(t) = \frac{\sum_{i=0}^{N-1} s_{ZI}(t - i\,\Delta t)}{N} \qquad (10).$$

As shown in the bottom graph of Figure 10, when p_{ZI} is high, a zero value of p_{HSGF} does not guarantee that the system is not damaged.

A possible way of handling this problem is to compute the persistence degree p_{SGF} of the *small gain* symptom considering only the time instants where it is observable. In order to maintain a statistically significant number of samples, the set $T_{NZ}(t)$ of the last N samples where s_{ZI} is false is considered and a persistence degree p_{NZSGF} of the *small gain symptom* *with non zero input* is defined as $p_{NZSGF}(t) = \frac{\sum_{t_i \in T_{NZ}(t)} S_{SGF}(t_i)}{N}$.

The mean value $t_d(t) = \frac{\sum_{t_i \in T_{NZ}(t)} (t - t_i)}{N}$ represents the age of the set of observability of small gain faults.

The p_{NZSGF} and t_d values computed during the experiment of Figure 10 are shown in the upper two plots of Figure 11.

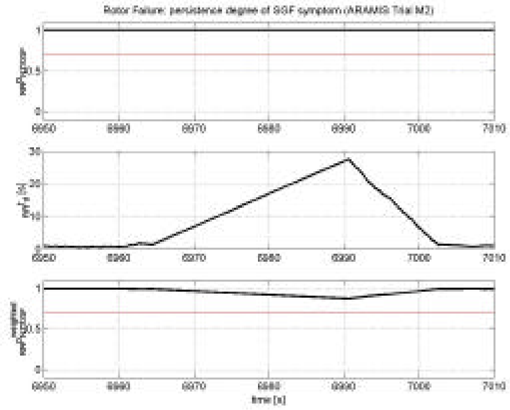

Figure 11. Vertical rear right rotor failure during ARAMIS Aegean Sea mission. From top to bottom: persistence degree and observability interval age of the *small gain symptom with non zero input*, and persistence degree of the *small gain* symptom with exponential decay.

Thus the persistence degree of the small gain symptom can be exponentially forgotten increasing the age of the observability interval as it follows:

$$p_{NZSGF}^{weighted}(t) = p_{NZSGF}(t) e^{-\frac{t_d - t_0}{t_c}}$$

where t_0 represents the minimum observability set delay, i.e. $t_0 = \frac{\sum_{i=0}^{i=N-1} (t - i\Delta t)}{N}$, and t_c is the system time constant. A fault alarm $f_{SGF}(t)$ at time t is generated if $p_{NZSGF}^{weighted}(t) > p_{NZSGF}^{thr}$. Results for t_c = 200 s are shown in the bottom plot of Figure 11, where the exponential decay of the persistence degree of the small gain symptom is clearly visible. The supervision module, e.g. the ROV human operator, is provided with a small gain fault alarm also for some time after that a zero input signal is applied to the system.

Fault detection and diagnosis: experimental results

The fault detection and diagnosis method through servo-amplifiers I/O monitoring discussed in the previous section has been applied to a large number of telemetry data collected during Romeo's at sea missions. In the following attention will focus on a couple of trials, where actuator failures verified.

Figure 12. VEFL thruster flooding in Antarctic mission.

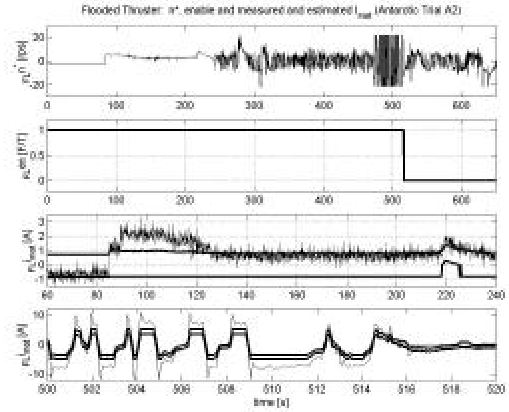

Figure 12a. Flooded thruster behavior. From top to bottom: reference propeller revolution rate, thruster enable and measured and expected motor current in a couple of regions of interest.

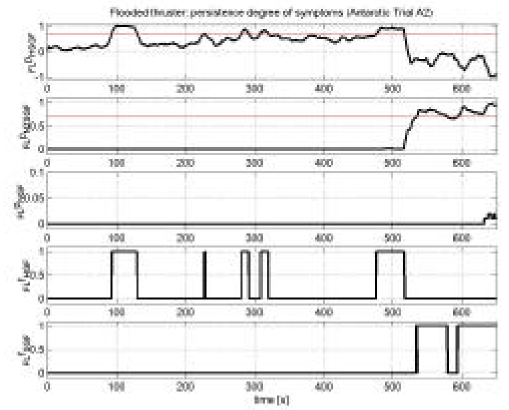

Figure 12b. Fault detection and diagnosis: flooded thruster. From top to bottom: persistence degree of the *high-small gain* symptom, *small gain* symptom with exponential decay, and *negative gain* symptom, and *high* and *small gain* fault alarms.

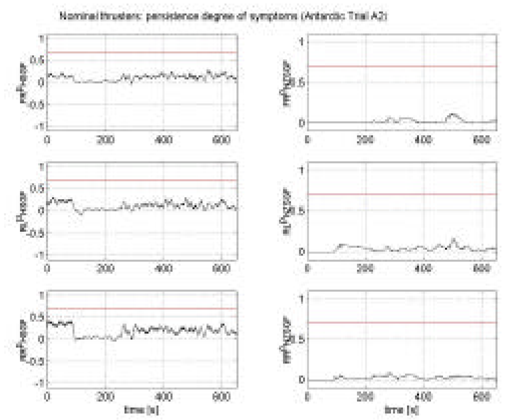

Figure 12c. Fault detection and diagnosis: nominal thrusters. Persistence degree of the *high-small gain* symptom (left column) and *small gain* symptom with exponential decay (right column).

Antarctic Trial A2

During the execution of an under-ice mission in Terra Nova Bay, the Romeo's vertical front left thruster flooded, while the other three vertical actuators worked in nominal conditions.
As shown in the top plot of Figure 12a, after about 90 s the vehicle started to submerge (a positive propeller revolution rate was required).Then at time about equal to 240s, auto-depth was switched on. As a consequence of the flooded thruster the depth controller reached a limit cycle around time 480 s, and the pilot disabled the vertical front left actuator after 516 s (see the second plot from the top of Figure 12a). The combined effects of the time-varying and low observable at low speed nature of the high gain fault are clearly visible in the third plot of Figure 12a, where a particular of the measured and expected motor current is shown, and in the diagnosis results of Figure 12b, where high-gain fault alarms are generated in correspondence of high module reference speed. Fault detection and diagnosis results of Figure 12b show the correct small gain fault diagnosis when the flooded thruster is disabled. Persistence degree of symptoms for the actuators working in nominal conditions are plotted in Figure 12c.

ARAMIS Trial M1

During the exploration of the ARAMIS test site in the thermal vent area of the island of Milos, the rotor of the vertical rear right thruster was damaged; in this case, an occasional fault, due to an unsteady contact in the connector of the vertical front left actuator verified too.

Figure 13. Vertical rear right rotor failure during ARAMIS Aegean Sea mission.

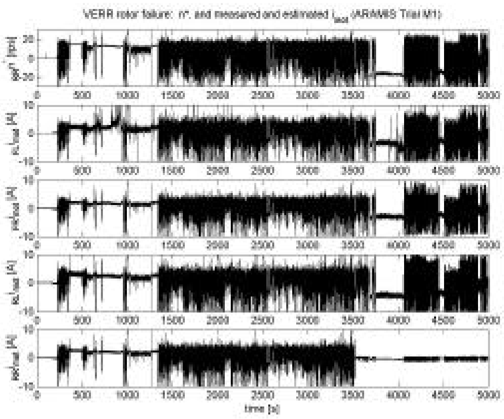

Figure 13a. From top to bottom: reference propeller revolution rate and measured motor currents.

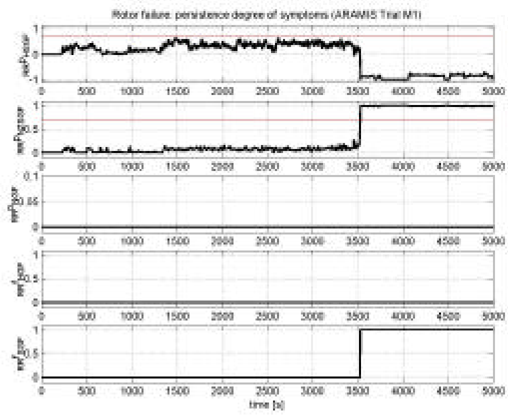

Figure 13b. Fault detection and diagnosis: damaged-rotor thruster. From top to bottom: persistence degree of the *high-small gain* symptom, *small gain* symptom with exponential decay, and *negative gain* symptom, and *high* and *small gain* fault alarms.

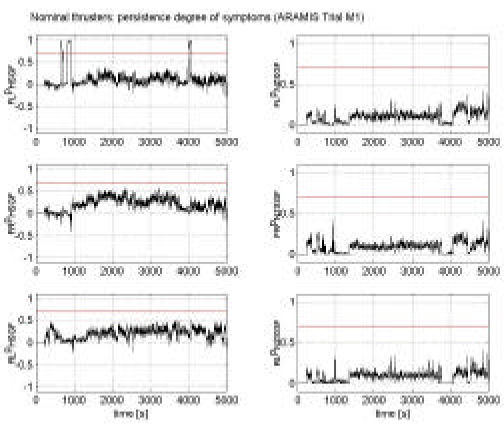

Figure 13c. Fault detection and diagnosis: nominal thrusters. Persistence degree of the *high-small gain* symptom (left column) and *small gain* symptom with exponential decay (right column). Occasional high gain fault in the vertical front left thruster is clearly visible.

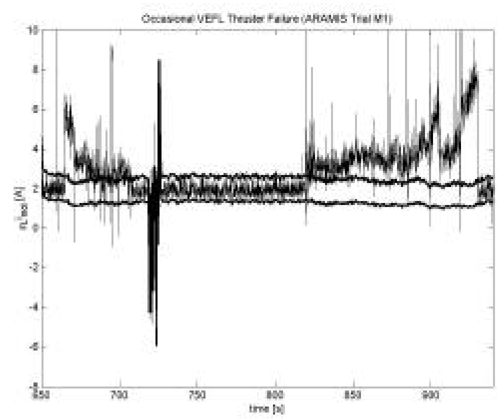

Figure 13d. Occasional vertical front left thruster failure. Measured and expected motor current.

As shown in Figure 13a, where the measured motor currents are plotted, the vertical rear right actuator damaged after about 3500 s, and the fault was immediately detected and isolated (see Figure 13b). The analysis of the persistence degree of symptoms for the actuators working in nominal conditions, see Figure 13c, revealed the presence of an occasional high-small gain fault in the vertical front left thruster. Further investigations carried out in the lab demonstrated the presence of an unsteady contact on the tachometer connector, which sometimes induced a zero velocity feed-back effect quite similar to the flooded thruster behavior. A particular of the vertical front left expected and measured motor current is plotted in Figure 13d, where the time-varying nature of the fault is pointed out.

Fault Accommodation

As discussed in [12] the fault-tolerant configuration of the Romeo's actuation system allows the reconfiguration of the Thrust Control Matrix in case of one vertical and/or horizontal thruster failure in a transparent way for the vehicle's control system in conventional operating conditions (only the maximum force and torque are reduced). Referring to Figure 2, calling α the module of the angle between the horizontal thrusters and the vehicle's longitudinal axis, b,c and d the thruster arms with respect to the vehicle center of mass respectively for yaw, roll and pitch motion, the horizontal and vertical Thrust Control Matrixes, relating the thruster forces $\tau_H = [\tau_{HFL} \quad \tau_{HFR} \quad \tau_{HRL} \quad \tau_{HRR}]^T$ and $\tau_V = [\tau_{VFL} \quad \tau_{VFR} \quad \tau_{VRL} \quad \tau_{VRR}]^T$ to the 6 DOFs force and torque $\phi_H = [F_u \quad F_v \quad T_r]^T$ and $\phi_V = [T_p \quad T_q \quad F_w]^T$, are

$$B_H = \begin{bmatrix} \cos\alpha & \cos\alpha & -\cos\alpha & -\cos\alpha \\ \sin\alpha & -\sin\alpha & \sin\alpha & -\sin\alpha \\ b & -b & -b & b \end{bmatrix}$$

and

$$B_V = \begin{bmatrix} -c & c & -c & c \\ -d & -d & d & d \\ 1 & 1 & 1 & 1 \end{bmatrix}$$

respectively.

A general purpose "optimal" distribution of the control actions consists in minimizing the quadratic energy cost function $J = \frac{1}{2}\tau^T P \tau$, which, in the case all inputs are equally weighed, has the solution $B^\# = B^T \left(BB^T\right)^{-1}$, known as Moore-Penrose pseudo-inverse [18]. When an actuator fault is diagnosed , the thruster is disabled, and the corresponding TCM reduces to a square matrix. Thus $B^\#$ is simply equal to B^{-1}, and the unique solution is computed.

The fault-tolerance of the Romeo's actuation system was demonstrated by the execution of about three hours of at sea work in reduced actuation configuration during the shallow water benthic trials of the ARAMIS project in thermal vent area near the island of Milos. An example of the performances in terms of precision in vertical motion estimation and motion control of the vehicle's operating with the vertical rear right thruster disabled is given in Figure 14, where the measured, estimated (through a model-based extended Kalman filter [12]), and reference depth are plotted.

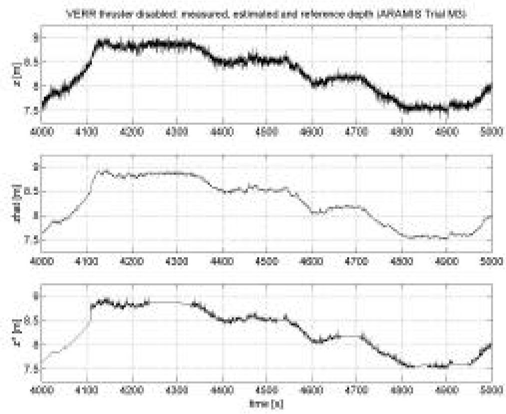

Figure 14. Shallow water ARAMIS Aegean Sea benthic mission with the vertical rear right thruster disabled. From top to bottom: measured, estimated and reference depth.

Conclusions

After having discussed the behavior of a ROV in presence of actuator faults during operating missions, the research presented in this paper demonstrated that low cost, efficient and reliable fault detection and diagnosis for ROV actuators can be performed by monitoring the I/O variables of the DC motor servo-amplifiers. The suitable processing of these data provides the human operator with sufficient information to make decisions about the reconfiguration of the actuation system. Considering the development of an AUV-oriented system, it is worth noting that the development of a robust and reliable automatic FDDA module has to face the time-varying, and sometimes occasional, nature of the experienced failures, and their observability according to the vehicle's maneuvers. The UUV's mission could be temporarily stopped to execute a set of pre-defined steady-state maneuvers specifically designed to solve ambiguities, and the nominal thrust control mapping could be periodically selected even if a fault-based reconfiguration has been accomplished in order to check the persistency of the detected fault.

Acknowledgments

This work has been partially supported by the Programma Nazionale di Ricerche in Antartide under Project 5.a.5 - Robotica e Telescienza in Ambiente Estremo, and by the Commission of the European

Community under Contract No. MAS3-CT97-0083 (Project ARAMIS).

References

[1] A.J.Healey, "Analytical redundancy and fuzzy inference in AUV fault detection and compensation", in *Proc. of Oceanology*, Brighton, UK, 2000, pp. 45-50.

[2] G.J.S. Rae, and S.E. Dunn, "On-line damage detection for autonomous underwater vehicles in *Proc. of IEEE 1994 Symposium on Autonomous Underwater Vehicle Technology*, Cambridge, USA, 1994, pp. 383-392.

[3] A. Orrick, and M. McDermott, "Failure detection in an autonomous underwater vehicle", in *Proc. of IEEE 1994 Symposium on Autonomous Underwater Vehicle Technology*, Cambridge, USA, 1994, pp. 377-382.

[4] A.J. Healey, "Optimal fault detection and resolution during maneuvering for AUVs", in *Proc. of 5th IFAC Symposium on Manoeuvring and Control of Marine Craft*, Aalborg, Denmark, 2000, pp. 17-26.

[5] K.C.Yang, J. Yuh and S.K. Choi, "Experimental study of fault-tolerant system design for underwater robots", in *Proc. of the 1998 IEEE International Conference on Robotics and Automation*, Leuven, Belgium, 1998, pp. 1051-1056.

[6] Alessandri, A., M. Caccia and G. Veruggio, "Fault detection of actuator faults in unmanned underwater vehicles", in *Control Engineering Practice*, Vol. 7, No. 3, pp. 357-368, 1999, Elsevier Science Ltd.

[7] Alessandri A., Bruzzone G., Caccia M., Coletta P., Veruggio G., "Fault detection through dynamics monitoring for unmanned underwater vehicles", in *Proc. of 4th IFAC Symposium on Fault Detection Supervision and Safety for Technical Processes*, Budapest, Hungary, 2000, vol. 2, pp. 973-978.

[8] K.P. Valavanis, D. Gracanin, M. Matijaševic, R. Kolluru, G.A. Demetriou, "Control Architectures for Autonomous Underwater Vehicles", in *IEEE Control Systems Magazine*, vol. 17, no. 6, 1997, pp. 48-64.

[9] M. Caccia, R. Bono, G. Bruzzone, G. Veruggio, “Variable Configuration UUVs for Marine Science Applications”, *IEEE Robotics and Automation Magazine*, Vol. 6, No. 2, June 1999, 1998, pp. 37-50.

[10] M. Caccia, "ARAMIS - Results of the tests with medium size ROV", *C.N.R.-I.A.N. Technical Report* no. 388, Genoa, Italy, 2000.

[11] R. Bono, Ga. Bruzzone, Gi. Bruzzone, M. Caccia, "ROV actuator fault diagnosis through servo-amplifiers' monitoring: an operational experience", in *Proc. of MTS/IEEE Oceans’99*, vol. 3, pp. 1318-1324, Seattle, USA, 1999, pp. 13-16.

[12] M. Caccia, and G. Veruggio, "Guidance and control of a reconfigurable unmanned underwater vehicle", *Control Engineering Practice*, Vol. 8, no. 1, 2000, pp. 21-37, Elsevier Science Ltd.

[13] M. Nokin (1998). “Sea trials of the deep scientific system Victor 6000”, in *Proc. of Oceans’98*, Nice, France, 1998, vol. 3, pp. 1573-1577.

[14] W.J. Kirkwood, “Tiburon: Science and Technical Results from MBARI’s New ROV Integrated to a SWATH Platform”, in *Proc. of Oceans’98*,. Nice, France, 1998, vol. 3, pp. 1578-1583.

[15] M.Caccia, R. Bono, G. Bruzzone, G. Veruggio, "Unmanned Underwater Vehicles for scientific applications and robotics research: the ROMEO Project", in *Marine Technology Society Journal*, Vol. 24, n. 2, 2000, pp. 3-17.

[16] M. Caccia, G.Indiveri, G.Veruggio, "Modelling and identification of open-frame variable configuration unmanned underwater vehicles", in *IEEE Journal of Oceanic Engineering*, vol. 25, no. 2, 2000, pp. 227-240.

[17] D. Theilliol, D. Sauter and L.G. Vela Valdes, "Integration of qualitative and quantitative methods for fault detection and isolation", in *Proc. of Safeprocess’97*, Hull, UK, 1997, vol. 2, pp, 687-692.

[18] T. I. Fossen, *Guidance and Control of Ocean Vehicles*, John Wiley & Sons, England, 1994.